RSC Advances

PAPER

View Article Online
View Journal | View Issue

Cite this: *RSC Adv.*, 2020, **10**, 38120

Synergistic lignin construction of a long-chain branched polypropylene and its properties

Bo Tian,[ab] Jinfeng Li,[b] Zhigang Li,[b] Ningdi Xu,[d] Gang Yao,[b] Nan Zhang,[b] Wei Dong,*[c] Yuguang Liu*[b] and Mingwei Di*[a]

Received 10th August 2020
Accepted 20th September 2020

DOI: 10.1039/d0ra06889f

rsc.li/rsc-advances

In light of current environmental pressures (referring to its destruction) and the consumption of petrochemical resources, the substitution of chemicals products with renewable natural substances has attracted extensive interest. In this paper, a synergistically constructed lignin polypropylene matrix composite with long-chain branched characteristics was prepared by a pre-irradiation and melt blending method. The effects of lignin on the crystallization, rheological behavior, foaming and aging properties of polypropylene were studied. Differential scanning calorimetry and polarized light microscopy results show that lignin undergoes heterophasic nucleation in a polypropylene matrix; rheological studies show that lignin promotes the formation of a heterogeneous polypropylene network, and thus polypropylene exhibits long-chain branching features; nucleation and a network structure endow the polypropylene-based composites with uniform cell size, thin cell walls, and a foaming ratio of 5–44 times; at the same time, a large number of hindered phenols in lignin can capture free radicals to improve the aging properties of the polypropylene. This research will help to convert industrial waste into functional composite materials.

Introduction

Polypropylene (PP), one of the top five synthetic resins, has been widely used in many fields due to its excellent mechanical and processing properties.[1–5] However, PP with a semi-crystalline linear structure has poor toughness, a low melt strength, and difficulty in thermoforming processing, limiting its use in high-value-added engineering applications such as in the automobile, construction, and packaging industries.[6–9]

Generally, in order to improve the melt strength of polyolefin, a great deal of effort has been devoted to introducing long-chain branches and hydrogen bonds into the polymer network.[10–13] Li *et al.*[14–16] grafted the long-chain monomer glycidyl methacrylate onto the PP molecular chain to improve the melt strength of PP, while improving its crystallization performance and toughness; Yoshii *et al.*[17–20] prepared high-melt-strength PP (HMSPP) by adding multifunctional monomers using an electron beam and γ-ray irradiation methods. However, the network structure formed by introducing long branches is easy to cross-link, and so is difficult to reuse. The hydrogen bonding network structure not only improves the melt strength and compatibility, but also solves the problem that the chemical graft molecular structure cannot be disassembled.[21–24] However, there are few reports on improving the melt strength of polypropylene by introducing hydrogen bonds. In the previous work of our research group, by adding acrylamide (AM) to form intermolecular hydrogen bonds, the compatibility of the two latex particles of different polarities with PP, and the melt strength of PP, were improved. However, due to the low concentration of hydrogen bonds formed by AM and the weak polarity of the PP blends, the compatibility of the polar latex particles with PP needs to be further promoted. The polar natural polymer lignin molecule contains a large number of hydroxyl groups that can form intramolecular and intermolecular hydrogen bonds,[25] which can cooperate with AM to construct a PP network and improve the melt strength of PP. Lignin is considered to be a physical cross-linking point in the PP matrix, improving the heterophasic nucleation of PP.[24,26] The hindered phenol structural unit in the lignin can stabilize free radicals and has a stabilizing effect on the active sites on the PP molecular chain, where no grafting reaction occurs, and it can also inhibit PP degradation and chain scission, promoting its aging performance.[27–31]

In this study, PP-based composite materials containing PP, lignin sulfonate (LS), carboxylated nitrile rubber emulsion (xNBR) and the water-soluble monomer acrylamide (AM) were prepared by pre-irradiation and melt blending (PP/xNBR/AM/LS). We have studied the effects of lignin on the crystallinity,

[a]*Key Laboratory of Bio-Based Material Science and Technology (Ministry of Education), Northeast Forestry University, Harbin 150040, China. E-mail: dimingwei@126.com*
[b]*Institute of Technical Physics, Heilongjiang Academy of Science, Harbin, 150086, P. R. China. E-mail: ygliu_63@163.com*
[c]*Institute of Radiation Medicine, China Academy of Medical Science, Peking Union Medical College, Tianjin 300192, P. R. China. E-mail: dongwei@irm-cams.ac.cn*
[d]*Harbin Institute of Technology, Harbin, P. R. China*

rheological properties, foaming properties and the aging of the composite materials.

Experimental section

Materials

PP (T30 S), melt flow rate is 2.8 g/10 min, China National Petroleum Daqing Refining and Chemical Plant; xNBRL (FM301), solid content 41 wt%, combined nitrile content ≥30, was obtained from Feima Chemical Co., Ltd. (Xinxiang, China); AM, (C_3H_5NO) ≥98 wt%, PH 5.5–7.5, Tianjin Kermel Chemical Reagent Co., Ltd.; LS, 65 wt%, Shenyang Xingzhenghe Chemical Co., Ltd.; Antioxidant Irganox1076, China Nanjing Milan Chemical Co., Ltd.; carbon dioxide with a purity of 99.95% was used as a blowing agent.

Pre-irradiation

A ^{60}Co-γ-ray ionizing irradiation device (3.7×10^{15} Bq) was used. The PP powder was packed into a PE bag, the irradiation dose was set to 0.2 kGy, and irradiation was carried out for 4 hours, and the sample marked as rPP. xNBRL was put into a PET bottle, the irradiation dose was set to 250 kGy, and irradiation was carried out for 12.5 hours, with the sample marked as rxNBRL.

Composite material preparation

PP, AM and LS were placed into the high-speed mixer according to the ratio, mixed evenly and put into the torque rheometer (RM200C), the temperature was set to 30 °C, and then rxNBRL was added at a speed of 60 rpm. After fully kneading for 10 minutes and raising the temperature to 185 °C at 15 °C min^{-1}, rPP and an antioxidant were added to react to torque balance. The sample numbers and the experimental formulae are listed in Table 1. For the schematic diagram of the melt structure, see Scheme 1.

Characterization

Differential scanning calorimetry (DSC) and Q200 (US TA) were used to test the crystallization performance of the samples. 5–10 mg of the sample was placed in the crucible, heated up to 50 °C, held for 1 min, kept at a constant temperature of 50–200 °C for 5 min, cooled to 50 °C at a temperature drop rate of 10 °C min^{-1}, and held for 1 min. Then, the temperature was raised to 200 °C at a rate of 10 °C min^{-1}. The melting enthalpy was calculated according to the melting peak area, and the crystallinity of the composite material was calculated according to the following formula of X_c,

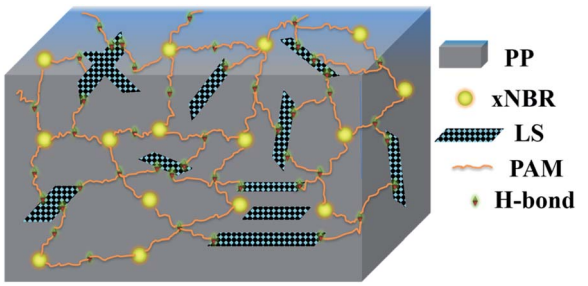

Scheme 1 Schematic diagram of the PP-based composite melt structure.

$$X_c = \frac{\Delta H_m}{f \Delta H_m^0} \times 100\% \quad (1)$$

in which the enthalpy of fusion of 100% crystalline PP is 209 J g;[32] ΔH_m is the melting enthalpy of the PP-based composite material, and f is the volume fraction of PP in the composite material. Polarizing microscopy (PLM) and XPV-400E (Shanghai Changfang Optical Instrument Co., Ltd., China) were used to test the crystal morphology of the samples. The samples were melted at 190 °C for 5 min, then annealed at 135 °C, maintained at a pressure of 10 MPa for 2 h, and then hot pressed into a 100 μm film. A rotating rheometer, Physica MCR102 (Austria Anton Paar GmbH) was used to test the rheological properties of the samples. Using dynamic scanning, the frequency was set to (ω) 100 to 0.05 rad s^{-1}, the strain (γ) at 1%, the temperature was set at 200 °C, and the sample was made into a cylindrical sheet with a diameter of 2.5 mm and a thickness of 1 mm. The foaming experiment was carried out using a self-made foaming device in the laboratory. 1.5 g of the sample was taken and filled with liquid CO_2 for 10 min, whilst the foaming temperature was between 155–165 °C, the pressure was 20 MPa, and the holding time was 2–4 h in 2 s. The autoclave was depressurized internally and the sample was put into ice water to cool to room temperature. The formula for calculating the cell density of the PP-based composites is,

$$N = \left(\frac{nM^2}{A}\right)^{3/2} \quad (2)$$

in which N is the cell density, n is the number of cells in the photomicrograph, M is the magnification of the photomicrograph,

Table 1 Mass percentages of PP-based composite materials

Sample	PP (wt%)	xNBRL (wt%)	AM (wt%)	LS (wt%)	rPP (wt%)	Antioxidant1076 (wt%)
PP	99	0	0	0	0	1
PP1	94	5	0	0	0	1
PP2	84	5	5	0	5	1
PP3	83	5	5	1	5	1
PP4	82	5	5	2	5	1
PP5	79	5	5	5	5	1

and A is the area of the photomicrograph (cm^2). The formula for calculating the average cell diameter is,

$$D = \frac{\sum d_i n_i}{\sum n_i} \quad (3)$$

where D is the average cell diameter, n is the number of cells, and d is the perimeter-equivalent diameter of the cells (i is greater than 200). The needle density drainage method was used to test the apparent density before and after foaming. The formulae for the expansion ratio and the bubble ratio are,

$$\phi = \frac{\rho}{\rho_f} \quad (4)$$

$$V_f = 1 - \frac{\rho_f}{\rho} \quad (5)$$

where ϕ is the expansion ratio, ρ is the density before foaming, ρ_f is the density after foaming, and V_f is the bubble ratio.[33] The morphology of the foaming sample was observed with a scanning electron microscope (SEM), JSM-IT300LV (JEOL corporation of Japan). The sample was dipped into liquid nitrogen for 5 min to be quenched, and then glued to the aluminum sheet with a conductive adhesive. For thermogravimetric analysis (TGA), TGA5500 (us waters), 5–10 mg of the sample was put into a dry pot, and data was recorded at a temperature of 25–800 °C.

Results and discussion

Analysis of the crystallization performance

The crystallization curves and melting curves of the PP-based composites with different components are shown in Fig. 1A and 1B. The DSC test results and the thermal performance parameters of the composite materials are shown in Table 2.

In Fig. 1A of the crystallization curve, compared with PP, the PP1 crystallization peak is shifted towards the high temperature zone, because of the interfacial effect of PP and xNBR, and the data shows that the initial crystallization temperature (T_i), crystallization temperature (T_c), and Xc increased and the supercooling degree (ΔT) decreased (Table 2), indicating that the xNBR particles affected the crystallization of PP. The crystallization morphology is shown in Fig. 1C and D. After the addition of AM, the intermolecular hydrogen bonds formed by AM with PP and xNBR formed PP-*g*-PAM and xNBR-*g*-PAM, respectively, improving the compatibility of PP and xNBR, and resulting in enhanced interfacial action, a faster crystallization rate, lower crystallization integrity, as shown in Fig. 1E, and enhanced heterogeneous nucleation. Thus, the PP2 crystallization peak moved significantly towards the high temperature region.

Table 2 Thermal performance parameters of the PP-based composites

Sample	T_c (°C)	T_m (°C)	ΔT ($T_m - T_c$)	ΔH_m (J)	T_i (°C)	X_c (%)
PP	114.58	163.15	48.57	56.47	118.44	0.27
PP1	115.34	163.25	47.91	89.82	120.27	0.45
PP2	126.54	165.96	39.42	94.29	130.85	0.50
PP3	129.57	166.74	37.17	96.18	133.73	0.52
PP4	130.46	166.80	36.34	91.75	134.53	0.50

When xNBR and AM additions were fixed, the intermolecular hydrogen bond concentration increased with increasing LS. T_i and T_m increased, ΔT decreased, the crystallization rate accelerated, and the crystallization integrity further decreased, indicating that LS has a heterophase nucleation effect.[34] When the LS content reached 5 parts of PP5, the crystallization peak shifted towards low temperature and T_i, T_c and X_c decreased, indicating that excessive LS hinders the crystallization and growth of the PP substrate (Fig. 1F). As shown in Fig. 1B, the melt curve showed that the composite has a typical α-crystallization melt peak at 165 °C. The PP5 curve not only has a typical α-crystallization melt peak at 165 °C, but it also has a small peak at 152 °C, corresponding to β-crystallization. That is, LS has a certain induction effect on the crystallization process of the β-crystallization of polypropylene.[35]

Rheological behavior of the composite melts

Shear rheology is very sensitive to the topology of the long-chain branched characteristic of PP molecular chains.[36] As can be seen from Fig. 2A, PP showed typical Newtonian fluid

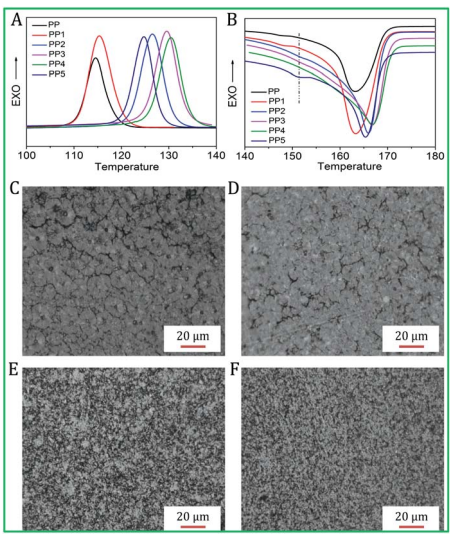

Fig. 1 Crystallization (A) and melting curves (B) of PP; POM diagrams of the polypropylene matrix composites: PP (C), PP1 (D), PP2 (E) and PP5 (F).

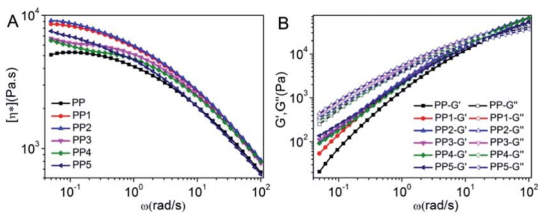

Fig. 2 Polypropylene matrix composite [η^*]–ω curves (A), and G' and G''–ω curves (B), with the low-frequency energy storage modulus (G') and low-frequency.

characteristics, and the Newtonian platform appeared in the low-frequency region. The complex viscosity (η^*) decreased with increasing frequency (ω) because the PP molecular chains undergo untwisting and orientation under shear stress. η^* is higher at the low-frequency end of the PP1 curve than in the PP curve because the xNBR particles are enhanced by binding to the PP interface, limiting the movement of the PP molecular chains and making η^* larger. The η^* value for the PP2 curve, introduced by AM, is increased slightly compared to PP and PP1 because AM promotes the dispersion of xNBR particles in the PP matrix and the enhanced interfacial action increases the η^* value.

The value of η^* for the PP3–PP4 curve decreases continuously with increasing LS content, and is lower than PP1 and PP2, but the low frequency slope increases and shear dilution occurs. The low molecular weight of LS led to a decrease in η^*, while the synergy between LS and AM promoted the formation of a PP-based composite network structure. The η^* value of PP5 decreased at high frequencies, and was even lower than that of PP, but it was still higher at low frequencies than that of PP3 and PP4, and the shear dilution was more pronounced. The former is due to the low molecular weight of LS, which makes the η^* value of the system lower, and the latter is due to the increase in the concentration of hydrogen bonds in the composite materials, which makes the network structure between the xNBR particles and PP more dense and increases the relaxation time.

The loss modulus (G'') values of the PP3–PP5 curves of LS were higher than the other components, and the critical point frequency (ω_c) shifted towards the low-frequency region, as is shown in Table 3. According to the classical linear viscoelastic theory, the molecular chain of the linear polymer homogeneous system could be completely relaxed, and its characteristic low-frequency end rheology was in accordance with exponential law, *i.e.* the $G' \propto \omega^2$ and $G'' \propto \omega$ relationships.[37] The introduction of LS G' and G'' values is less ω-dependent, and the slope and ω_c of G' and G'' were also reduced, as shown in Table 3. This is because LS acts as a physical crosslinking point in the PP matrix, forming a network structure that limits the movement of PP molecular chains.[38]

As can be seen from Fig. 3A, the viscosity of PP1 increased compared to the viscosity of PP, the melt elasticity increased and the low-frequency end tanδ value decreased. The PP2 tanδ value continued to decrease in the low-frequency region due to the heterogeneous network structure formed by intermolecular hydrogen bonding in PAM. After the addition of LS, the physical crosslinking point was formed due to the heterogeneous nucleation of LS, which made the PP matrix more elastic, and the low-frequency end tanδ value decreased continuously.

Table 3 Modulus (G', G'') and frequency (ω) dependence of the PP-based composites

Sample	Slope of G'	Slope of G''	ω_c
PP	1.006	0.665	33.762
PP1	0.928	0.621	23.635
PP2	0.875	0.618	22.083
PP3	0.863	0.663	21.551
PP4	0.890	0.674	21.465
PP5	0.806	0.612	17.387

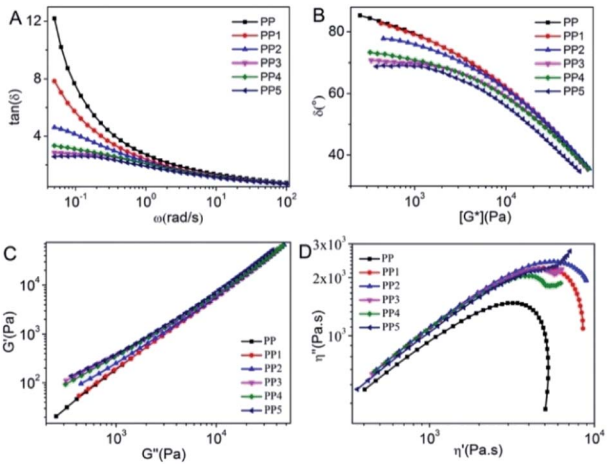

Fig. 3 tan(δ)–ω relationship of (A), relation between $\delta - G^*$ (B), Han's curves (G'–G'', C) and Cole–Cole curves (η'–η'', D) of polypropylene-based composites.

The increase in elasticity of the PP matrix composites with increasing particle-matrix forces could also be analyzed by the van Gurp–Palmen plot method, *i.e.* the phase angle (δ)-complex modulus ($|G^*|$) relationship curve.[39,40] As shown in Fig. 3B, PP and PP1 showed typical characteristics of linear polymers, with the δ value decreasing with increasing monotone of $|G^*|$. Due to the introduction of AM increasing the interfacial action of xNBR and PP, the PP substrate elasticity increased, and the δ value of PP2 was lower than that of PP and PP1. The δ values of PP3–PP5 were further reduced after the addition of LS, indicating that LS facilitated the formation of a heterogeneous network structure, further enhancing the substrate elasticity.

Han's curves are usually used to study the compatibility of composites and, if the components are compatible, they have the same slope between the components, otherwise they are considered incompatible or phase separation systems. The degree of deviation between the G'/G'' curves is determined by differences in system compatibility, dispersion and platform modulus.[41] As shown in Fig. 3C, the difference between the G'/G'' ratio between PP and the other samples gradually increased with the increasing interaction of xNBR with the PP substrate. The slope of the PP3–PP5 curves increased significantly after the introduction of LS, indicating that the addition of LS produced a microscopic phase separation phenomenon. Cole–Cole curves are often used to characterize the viscoelasticity of polymers and to study heterogeneous polymer systems. When a double arc curve is present, it can be interpreted as a result of the coexistence of two relaxation processes with very different relaxation times.[14,42] When a network structure is present in a polymer melt, it will cause an imaginary number viscosity ($|\eta''|$) (*i.e.* elasticity) to increase and thus have a low-frequency relaxation behavior, which leads to a longer relaxation time. From this information, the upward warping of the low-

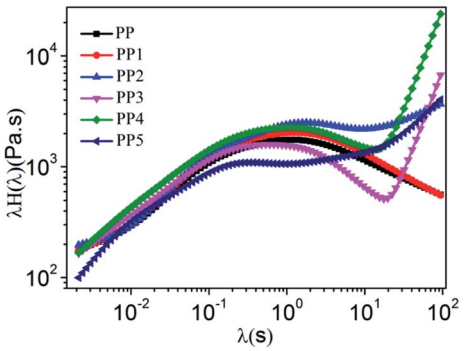

Fig. 4 The relaxation curves of PP at a temperature of 200 °C.

frequency region in the Cole–Cole diagram can be taken as a sign of the formation of a heterogeneous network structure.[43] It can be seen from Fig. 3D that when LS is introduced, the Cole–Cole diagram shows the phenomenon of low-frequency upwelling, indicating the formation of a heterogeneous network structure in the melt. With an increase in LS content, the interfacial effect was also enhanced, showing that the low-frequency upwelling was more pronounced, that is, it showed the heterogeneous structure of long-time hesitation.

In order to more clearly observe the polymer molecular chain relaxation phenomenon, the polypropylene matrix composite relaxation pulses were calculated from dynamic modulus data (G' and G''):

$$G'(\omega) = \int_{-\infty}^{\infty} \frac{H(\lambda)\omega^2\lambda^2}{1+\omega^2\lambda^2} \mathrm{d}\ln\lambda, \quad G''(\omega) = \int_{-\infty}^{\infty} \frac{H(\lambda)\omega\lambda}{1+\omega^2\lambda^2} \mathrm{d}\ln\lambda \quad (6)$$

$H(\lambda)$ in eqn (6) is the relaxation of PP, ω is the scan frequency, and λ is the PP molecular chain relaxation time.[44] The calculated relaxation is shown in Fig. 4. The PP and PP1 curves show one relaxation peak, which is characteristic of the relaxation of linear molecules, and PP2–PP5 show two relaxation peaks. The appearance of the second relaxation peak is a sign of the long-branched chain relaxation feature. PP2 has a second relaxation peak, indicating that PP2 has a long-chain branched feature. PP3–PP5 have a more pronounced second relaxation peak, where the chain motion of the system is more complex, indicating that LS promotes the formation of the PP heterogeneous network structure and has a more pronounced long-chain branched feature.

Foaming properties

Supercritical CO_2 was used to make the foam of the PP matrix composite material, and the cross-section SEM picture is shown in Fig. 5. It can be seen from Fig. 5A that, because the pure PP melt strength is low, the cell wall is thick and the cell is not uniform. Due to the small interaction between xNBR particles and the PP interface, the low melt strength, resulting in the PP1 pore size and the pore wall thickness, the pore rate was very low, so it was difficult to form stable pores, see Fig. 5B. In Fig. 5C, the addition of AM significantly improved the pore morphology of PP2, the pore walls were thinned, pore uniformity increased, and the pores underwent multi-deformation distribution. As the addition of AM enhances the interaction of xNBR particles with the PP interface, the melt strength increases, as shown in Fig. 5(D and E). The PP3 and PP4 pores with lignin added were more uniform in shape, with thin cell walls, in a polygonal arrangement and with elastic deformation of the cell walls, as the introduction of LS further strengthened the combination of the xNBR particles and PP, resulting in the strain hardening phenomenon.[45] Fig. 5F shows PP5 after adding 5 parts of LS. From the figure, it can be seen that the cell size decreased and the cell density increased, and that they are arranged in a polygon. On the one hand, the increase in LS increased the interface effect and the melt strength, and the toughness of the cell wall was increased, inhibiting the growth of the cell; on the other hand, LS had a heterogeneous nucleation effect, and the nucleation sites increased, which increased the cell density. This shows that adding LS made PP gain excellent foaming performance.

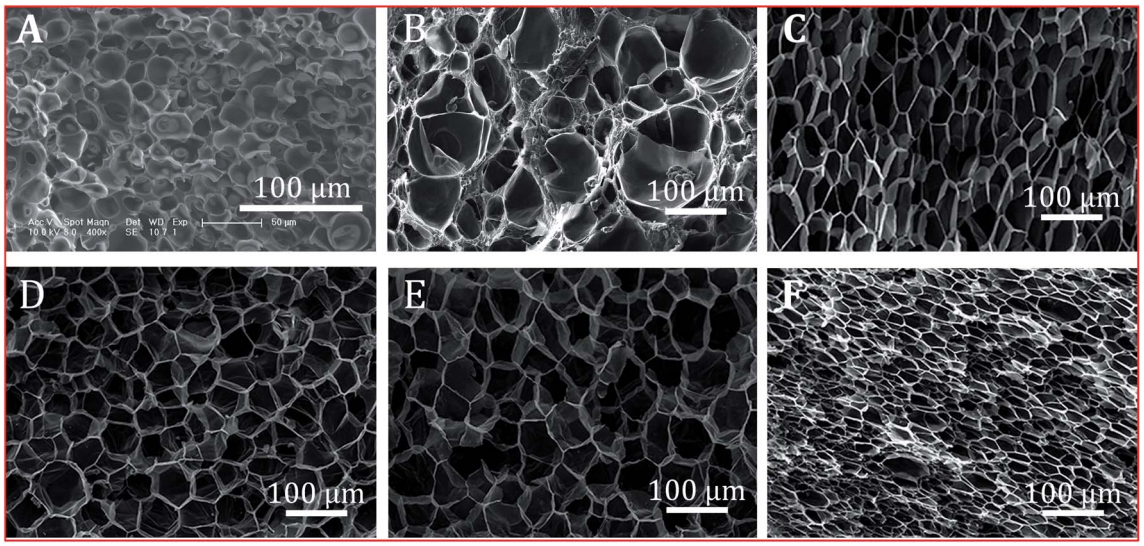

Fig. 5 Polypropylene-based composite foams: (A) PP, (B) PP1, (C) PP2, (D) PP3, (E) PP4, and (F) PP5.

Table 4 Cell densities of the PP-based composites (N), average cell diameters (D), foaming ratios (φ) and bubble ratios (V_f)

Sample	N (cells per cm^3) $\times 10^9$	D (μm)	φ	V_f (%)
PP	80	16	4.55	78.03
PP1	59	45	7.13	85.98
PP2	73	28	13.12	92.38
PP3	70	31	25.63	96.10
PP4	68	33	44.44	97.34
PP5	98	14	8.86	88.71

Table 4 shows the N, D, φ and V_f values of the samples corresponding to Fig. 5. It can be seen from Table 4 that, compared with PP, the N value decreased and D value increased in PP1 with xNBR, while the N value increased and D decreased in PP3 with AM, whilst the foaming performance was improved because AM improved the heterogeneous nucleation of PP. When the content of AM was fixed, with an increase in LS content, N first decreased and then increased, whilst D showed the opposite trend of first increasing and then decreasing, because the foaming performance is not only related to the heterogeneous nucleation, but it is also related to the melt strength, and the change in the law corresponds to the η^* and G' values in Fig. 2. The changes in the values for the PP composite material of φ and V_f were consistent with the changes of cell formation, stability and morphology, and it can be seen that under a certain LS content, the material had higher V_f and φ values, which were up to 44 times more, as can be seen in Table 4, and the change in the law and Fig. 5 results confirm each other.

Aging performance

The TGA thermal analysis curves of the PP matrix composites are shown in Fig. 6A. As the xNBR latex particles have good heat resistance and a certain interfacial bond with PP, the starting weightlessness temperature of PP1 was shifted towards high temperature, compared with the thermal decomposition curve of PP. The starting weight loss temperature of PP2 was lower than that of PP1, and this was caused by the volatilization of some small molecules by the addition of AM. Compared with PP2, PP4 and PP5 had a further lower starting weight loss temperature after the introduction of LS, and this was because of the low molecular weight of LS and the volatility of the introduced small molecules. The thermal decomposition rate (DTG) curves showed that the peak temperatures of PP1–PP5, with the additions of xNBR, AM and LS, were significantly higher than that of PP. However, the peak temperature increased after the introduction of LS was smaller than that of PP1 and PP2, because, on the one hand, the molecular weight of LS was low, whilst on the other hand, LS improved the interface effect, resulting in competition between the two.

The aging properties of the PP-based composites before and after γ-ray irradiation were evaluated by the changes of rheological parameters η^* and G'. Irradiation at low doses could simulate the aging properties of the materials for long periods

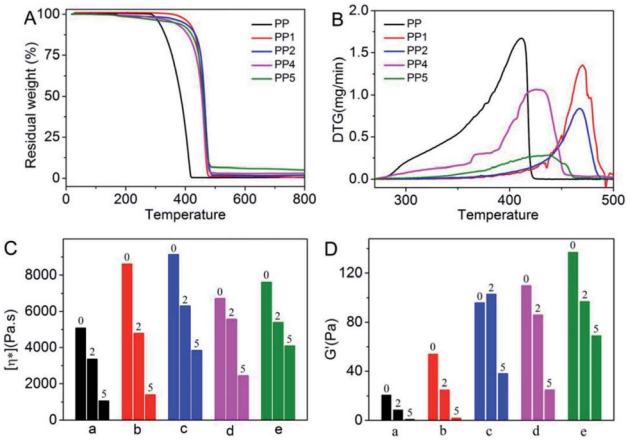

Fig. 6 TGA (A), DTG (B), radiation doses [η^*] (C) and G' retention rates (D) of the polypropylene-based composites. a, b, c, d and e represent PP, PP1, PP2, PP4 and PP5, respectively.

of time. The degradation of PP was free radical degradation, which was sensitive to γ-rays, and η^* and G' decreased sharply after irradiation; η^* and G' decreased significantly after PP1 irradiation, indicating that the xNBR particles were weakly bound to the PP interface and failed to inhibit PP degradation. The downward trend of η^* and G' of PP2 slowed down after irradiation, especially under 2 kGy irradiation, and G' increased slightly, due to the reduction of the PP molecular weight and the viscosity after irradiation. This further homogenized the xNBR latex particles in the PP matrix, on the one hand, and the introduction of AM, on the other hand, increased the interfacial action, forming a physical cross-linked network structure through hydrogen bonding and functional group action. Compared with PP2, the η^* and G' decreasing trend of PP4 irradiated at 2 kGy became smaller after the addition of LS, but the η^* and G' decreasing trend of PP5 increased with increasing LS content, indicating that the low molecular weight role of LS was greater than that involved in the formation of the heterogeneous network structures. With increased irradiation dose, the η^* and G' values of PP4 decreased significantly at 5 kGy irradiation, suggesting that the promoting effect of LS was much less than the degrading effect of the material. The η^* and G' values of PP5 still showed a decreasing trend with increasing LS content, however it was significantly higher than that of PP4, suggesting that the large number of hindered phenol structures in LS acted as stabilizing radicals. In addition, LS provides physical crosslinking points, making the network structure denser and slowing down the degradation of PP. In summary, LS slowed down PP free radical degradation and improved the PP aging performance.

Conclusions

In this paper, PP-based composites with long-chain branched features were prepared by pre-irradiation and melt blending through intermolecular hydrogen bonding. Crystallization performance studies showed that the addition of LS increased

the interfacial binding of xNBR particles to the PP matrix and provided a nucleation site, leading to T_i elevation, an increase in T_c and crystallization rate acceleration, whilst an increase in X_c showed a significant heterogeneous nucleation effect. By rheological characterization of the PP matrix composites with long-chain branched characteristics, the LS molecule rich in active groups promoted the formation of the PP network structure, resulting in a PP matrix with shear thinning characteristics, the relaxation time became longer and the relaxation behavior became complex. Due to the joint action of AM and LS, the PP matrix composites exhibited outstanding foaming performance, a uniform distribution of cells, thin cell walls like cicada wings, an increased density of cells, and a foaming multiplier up to 44 times. Aging performance analysis showed that LS had a good effect on inhibiting PP substrate β degradation, slowing down the degradation of PP and improving the aging performance. This work provides a multifunctional PP manufacturing method that opens new avenues for high value-added industrial lignin applications.

Conflicts of interest

There are no conflicts to declare.

Acknowledgements

This work was supported by the Natural Science Foundation for Youths of Heilongjiang Province of China (grant number QC2018070), the Heilongjiang Academy of Sciences Fund for Distinguished Young Scholars (grant number CXJQ2019WL01), and the Heilongjiang Academy of Sciences Fund for Pilot and Ripening Projects (grant number ZSSH2019WL01).

References

1 Y.-Y. Gao, C. Deng, Y.-Y. Du, S.-C. Huang and Y.-Z. Wang, *Polym. Degrad. Stab.*, 2019, **161**, 298–308.
2 Z. E. Nicole, G. Margaret, B. Zachary and G. Frank, *Addit. Manuf.*, 2019, **25**, 122–130.
3 P. Wu, Q. Yang, Z. Zhao, T. Zhang, Y. Huang and X. Liao, *Polymer*, 2019, **161**, 109–121.
4 A. Woźniak-Braszak, M. Knitter, E. Markiewicz, W. F. Ingram and R. J. Spontak, *ACS Sustainable Chem. Eng.*, 2019, **7**, 16050–16059.
5 H. F. Joaquín, R. Emilio, L. Juan and A. P. Marina, *Macromol. Mater. Eng.*, 2019, **304**, 1900379.
6 I. Bochkov, M. Varkale, R. Merijs Meri, J. Zicans, P. Franciszczak and A. Bledzki, *Green Tribology*, 2018, **1**, 4–8.
7 A. El-Sabbagh, T. Attia, A. Ramzy, L. Steuernagel and G. Ziegmann, *Composites, Part B*, 2017, **141**, 1–8.
8 M. Harris, J. Potgieter, S. Ray, R. Archer and K. Arif, *Materials*, 2019, **12**, 4167.
9 L. B. Canto, *Polym. Test.*, 2019, **73**, 135–142.
10 L. Pei, F. Liu, H. Liao, J. Gao, L. Zhong, H. Gao and Q. Wu, *ACS Catal.*, 2018, **8**, 1104–1113.
11 F.-h. Su and H.-x. Huang, *J. Supercrit. Fluids*, 2011, **56**, 114–120.
12 A. Shabbir, H. Goldansaz, O. Hassager, E. van Ruymbeke and N. J. Alvarez, *Macromolecules*, 2015, **48**, 5988–5996.
13 C. L. Lewis, K. Stewart and M. Anthamatten, *Macromolecules*, 2014, **47**, 729–740.
14 Y. C. Li, S. Jia, S. L. Du, Y. F. Wang, L. D. Lv and J. B. Zhang, *Waste Management*, 2018, **76**, 172–179.
15 H. J. Lee, J. W. Baek, T. J. Kim, H. S. Park, S. H. Moon, K. L. Park, S. M. Bae, J. Park and B. Y. Lee, *Macromolecules*, 2019, **52**, 9311–9320.
16 L. Fu, Q. Shi, Y. Ji, G. Wang, X. Zhang, J. Chen, C. Shen and C. B. Park, *J. Supercrit. Fluids*, 2020, **160**, 104794.
17 F. Yoshii, K. Makuuchi, S. Kikukawa, T. Tanaka, J. Saitoh and K. Koyama, *J. Appl. Polym. Sci.*, 1996, **60**, 617–623.
18 A. Lugao, B. W. H. Artel, A. Yoshiga, L. F. C. P. Lima, D. Parra, J. Bueno, S. Liberman, M. Farrah, W. R. Terçariol and H. Otaguro, *Radiat. Phys. Chem.*, 2007, **76**, 1691–1695.
19 R. Jiang, Y. Chen, S. Yao, T. Liu, Z. Xu, C. B. Park and L. Zhao, *Polymer*, 2019, **179**, 121628.
20 G. He, B.-Y. Yuan, T.-T. Zheng, W.-l. Zhu and X.-C. Yin, *RSC Adv.*, 2017, **7**, 22531–22539.
21 P. Westbye, T. Köhnke, W. Glasser and P. Gatenholm, *Cellulose*, 2007, **14**, 603–613.
22 P. a. Balázs, K. Dávid, R. Károly and P. a. Béla, *Int. J. Biol. Macromol.*, 2018, **107**, 1203–1211.
23 Y. Deng, X. Feng, M. Zhou, Y. Qian, H. Yu and X. Qiu, *Biomacromolecules*, 2011, **12**, 1116–1125.
24 H. J. Lee, H. K. Lee, E. Lim and Y. S. Song, *Compos. Sci. Technol.*, 2015, **118**, 193–197.
25 Q. Xia, Y. Liu, J. Meng, W. Cheng, w. chen, S. Liu, Y. Liu, J. Li and H. Yu, *Green Chem.*, 2018, **20**, 2711–2721.
26 L. N. Liu, M. B. Qian, G. B. Huang, Y. M. Yu and S. Y. Fu, *ACS Sustainable Chem. Eng.*, 2016, **4**, 2422–2431.
27 A. Beaucamp, Y. Wang, M. Culebras and M. Collins, *Green Chem.*, 2019, **21**, 5063–5072.
28 B. Waliszewska, M. Mleczek, M. Zborowska, P. Golinski, P. Rutkowski and K. Szentner, *Cellulose*, 2019, **26**, 6303–6315.
29 S. Chandna, N. S. Thakur, Y. N. Reddy, R. Kaur and J. Bhaumik, *ACS Biomater. Sci. Eng.*, 2019, **5**, 3212–3227.
30 G. F. Antonova, T. N. Varaksina, T. V. Zheleznichenko and A. V. Bazhenov, *Wood Sci. Technol.*, 2019, **53**, 927–952.
31 J. V. Vermaas, L. Petridis, J. Ralph, M. F. Crowley and G. T. Beckham, *Green Chem.*, 2019, **21**, 109–122.
32 Q. Guo, X. Li, W. Li and Z. Yao, *Ind. Eng. Chem. Res.*, 2018, **57**, 6696–6703.
33 W. Zhang, L. Yang, P. Chen, H. Zhang, W. Lin and Y. Wang, *Polym. Eng. Sci.*, 2013, **53**, 1598–1604.
34 S. Borysiak, Ł. Klapiszewski, K. Bula and T. Jesionowski, *J. Therm. Anal. Calorim.*, 2016, **126**, 251–262.
35 Y. Tian, J. Zhou and J. Feng, *Mater. Res. Express*, 2018, **5**, 045304.
36 Y. Li, C. Pan, Z. Xin, S. Zhou, X. Meng and S. Zhao, *J. Polym. Res.*, 2018, **25**, 46.
37 H. L. Xu, Y. H. Song, Q. X. Zhang and Q. Zheng, *Polymer*, 2018, **138**, 139–145.

38 J. Morshedian, M. Karbalaei-Bagher, H. Bayazian, A. Jamshidi and M. Razavi-Nouri, *Polym. Sci., Ser. A*, 2018, **60**, 523–529.
39 M. Kempf, V. Barroso and M. Wilhelm, *Macromol. Rapid Commun.*, 2010, **31**, 2140–2145.
40 Y. Li, Z. Yao, Z. H. Chen, S. L. Qiu, C. C. Zeng and K. Cao, *Ind. Eng. Chem. Res.*, 2013, **52**, 7758–7767.
41 L. Yang, T. Jiang, W. Gong, L. He, Z. Luo and C. Zhang, *Polym. Adv. Technol.*, 2018, **29**, 2300–2307.
42 H. Y. Liao, G. L. Tao, C. L. Liu and F. H. Gong, *J. Appl. Polym. Sci.*, 2016, **133**, 43709.
43 T. T. Yang, Y. W. Qin and J. Y. Dong, *Macromolecules*, 2018, **51**, 9234–9249.
44 D. Ismahane, K. Rachida, A. Nora, F. Mercedes and E. Agustin, *J. Elastomers Plast.*, 2018, **50**, 611–633.
45 C. G. Yang, Z. Xing, M. H. Wang, Q. Zhao, M. L. Wang, M. J. Zhang and G. Z. Wu, *Ind. Eng. Chem. Res.*, 2018, **57**, 15916–15923.